

Constant DC power infeed grid forming with improved ability to ride-through unbalanced low-voltage faults

Tayssir Hassan, Malte Eggers, Huoming Yang, Peter Teske, Sibylle Dieckerhoff

TECHNISCHE UNIVERSITÄT BERLIN

Chair of Power Electronics

Einsteinufer 19

10587 Berlin, Germany

Tel: +49 (0)30 314-25513

Email: t.hassan@tu-berlin.de

URL: <http://www.pe.tu-berlin.de>

Keywords

«Grid-connected converter», «Grid-forming converters», «Converter control», «Small signal stability», «Real-time simulation».

Abstract

A new optimized grid-forming control strategy based on matching control is presented, which can be used in an unbalanced system and provides minimum frequency support by utilizing the energy stored in the dc-link capacitor. Simulation and measurements in different scenarios and under asymmetrical grid faults evaluate the proposed strategy.

Introduction

In today's power grids, the contribution of renewable energy sources such as wind turbines and photovoltaic cells is increasing rapidly [8]. These sources are mainly connected to the power grid via power electronics converters, which usually operate in a grid-following manner. In this way, they feed the maximum available active power into the grid and act as a constant power source, independent of grid frequency fluctuations, which reduces the ability of the power grid to cope with frequency deviations[9]. To improve stability in grids with high penetration of power electronics, many grid-forming control strategies have been presented. One of these is the matching control, which is introduced in [1]. The matching control creates an equivalence between the energy stored in the dc-link capacitor to the rotational energy of a synchronous generator. This means that the dc-link voltage varies proportional to frequency variations. The authors of [2] modified this strategy to eliminate the steady-state dc-link voltage deviation and performed a stability analysis. In [3] the impact of reaching DC- and AC-current limitation has been investigated in addition to the interaction between the fast grid-forming converters and the slow synchronous machine dynamics.

This paper presents an optimized grid-forming control strategy based on the matching control, focusing on improving the performance of this strategy in the presence of unbalanced grid faults. Moreover, the effectiveness of using the dc-link capacitor to provide frequency support in a limited range is investigated, and the impact of this small inertia contribution to the distribution grid is studied.

A small-signal model helps to study the system stability and to determine the control parameters. For experimental verification, the control strategy is implemented in a test bench with three converters in parallel connected to a hardware-in-the-loop system. Several grid faults are applied, and their effects on the strategy are investigated.

The paper is organized as follows: The original matching control is discussed, highlighting its

weaknesses. Then, the proposed changes to this strategy are presented. Finally, the measurement results are introduced and evaluated.

The matching control strategy

The basic idea of the matching control strategy is to establish equivalence between the electrical energy stored in the dc-link capacitor to the rotational energy stored in the rotor of a synchronous generator. Considering the mathematical similarity between the differential equation of the DC capacitor and the swing equation of the synchronous generator. Equation (1) shows the swing equation

$$J_{SG} \cdot \omega_n \cdot \frac{d\omega}{dt} + D_{SG} \cdot \omega_n \cdot (\omega - \omega_n) = P_T - P_{ESG} \quad (1)$$

where J_{SG} is the inertia of the generator, ω is the rotational speed, ω_n is the synchronous rotational speed, D_{SG} is the damping constant, P_T is the mechanical power, and P_{ESG} is the electrical output power of the generator. The angular momentum at the synchronous speed is $M = J_{SG} \cdot \omega_n$ and $D = D_{SG} \cdot \omega_n$ is the damping constant at this speed.

The dynamic equation of the dc-link capacitor is presented in equation (2)

$$C_{DC} \cdot \frac{dV_{DC}}{dt} = i_S - i_E = \frac{P_s}{V_{DC}} - \frac{P_E}{V_{DC}} \implies \frac{C_{DC}}{2} \cdot \frac{dV_{DC}^2}{dt} = P_s - P_E \quad (2)$$

where P_s is the power delivered by the power source, i_S is the associated DC-current. P_E is the active power output of the converter with i_E as the corresponding DC-current.

According to the definition of the matching control, equation (1) and (2) are equal, by integrating equation (3) and applying the Laplace transform on it equation 4 is obtained.

$$M \cdot \frac{d\omega}{dt} + D \cdot (\omega_{SG} - \omega_n) = \frac{C_{DC}}{2} \cdot \frac{dV_{DC}^2}{dt} \quad (3)$$

$$\omega = \omega_n + \frac{s}{k_j \cdot s + k_d} \cdot (V_{DC}^2 - V_{DC,n}^2) \quad k_j = \frac{2 \cdot M}{C_{DC}} \quad k_d = \frac{2 \cdot D}{C_{DC}} \quad (4)$$

Equation (4) represents the relation between the rotational speed and the dc-link voltage. This relation is defined by a differential-controller which reacts to frequency deviation by controlling the dc-link voltage. In [2] equation (4) is modified to a proportional-differential (PD) controller as shown in equation (5),

$$\omega = \omega_{ref} + \frac{s + k_t}{k_j \cdot s + k_d} \cdot (V_{DC}^2 - V_{DC,n}^2) \quad \omega_{ref} = m \cdot \omega_{PLL} + (1 - m) \cdot \omega_n \quad (5)$$

where ω_{ref} is the reference angular frequency, ω_{PLL} is the angular frequency measured by the phased-locked loop (PLL), m is a weighting coefficient between 0 and 1 and k_t , k_d , k_j are the control parameters. The reference angular frequency ω_{ref} , is not a constant value, which helps to reduce the deviation of the dc-link voltage from its nominal value during frequency deviation. By using the new controller presented in [2], the dynamic equation of the dc-link capacitor becomes as follows:

$$(k_j C_{DC}/2) \cdot s \cdot \omega + (k_d C_{DC}/2) \cdot (\omega - \omega_{ref}) - (P_s - P_E) = (k_t C_{DC}/2) \cdot (V_{DC}^2 - V_{DC,n}^2) \quad (6)$$

If the rotational frequency equals its reference value, then the right side of equation (6) is zero and the dynamic equation of the dc-link capacitor matches the swing equation of the synchronous generator. However, this can only be achieved when the weighting coefficient m is equal to 1, which increases the influence of the PLL on the system. Therefore, the performance of the system under weak grid conditions is limited. Moreover, asymmetrical faults cause 100Hz power oscillation and thus lead to 100Hz output frequency oscillation [7]. Under this condition, the PLL may also suffer from stability issues that can cause the whole system to become unstable. The model presented in [2] has been extended and optimized to solve these problems and improve the behavior of the system under such conditions.

The optimized model

The proposed strategy provides a way to eliminate the dc-link voltage deviation without requiring a PLL, resulting in an overall better stability of the system. To achieve this, the PD-controller shown in equation (5) is replaced by a proportional-integral-differential (PID) controller, which ensures zero steady state error of the dc-link voltage. In addition to the new controller, a notch filter is integrated into the control system to eliminate the aforementioned frequency oscillation during unbalanced faults.

$$\omega = \omega_n + \frac{s^2 + k_1 \cdot s + k_2}{k_3 \cdot s \cdot (s + k_4)} \cdot (V_{DC}^2 - V_{DC,n}^2) \quad (7)$$

where k_1 , k_2 , k_3 and k_4 are the control parameters. With the new control strategy, the dynamic equation of the dc-link capacitor is shown in equation (8).

$$\underbrace{(1/k_2) \cdot s \cdot \omega - (k_1/k_2) \cdot (\omega - \omega_n) - (P_S - P_E)}_{\text{Grid synchronization unit}} = \underbrace{(1/k_2) \cdot (k_3 + k_4 \cdot \frac{1}{s}) \cdot (V_{DC}^2 - V_{DC,n}^2)}_{\text{dc-link voltage controller}} \quad (8)$$

During steady-state, the right side of equation (8) is always zero, which ensures a zero deviation of the dc-link voltage even during frequency deviation.

Fig. 1 shows the block diagram of the control system. The dc-link voltage controller block combined with the grid synchronization unit, represent the dynamics of the dc-link capacitor shown in equation (8). The reactive current droop block, consists of the $-i_Q \sim V$ -droop as proposed in [4], and a PI-

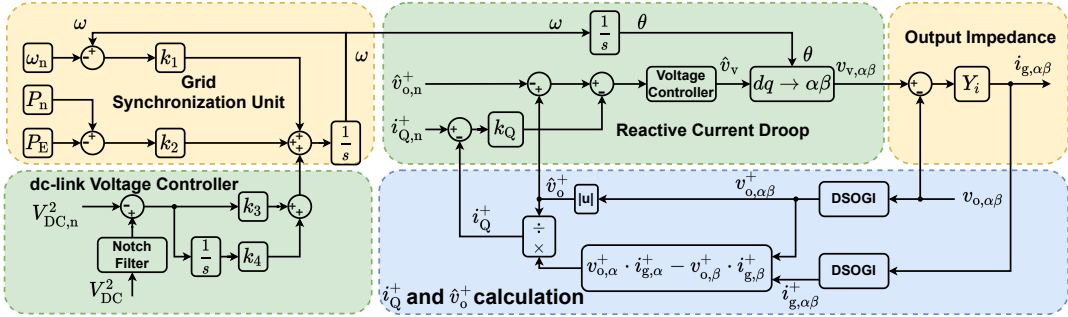


Fig. 1: Block diagram of the control strategy

voltage controller that sets the virtual internal voltage to regulate the reactive current. The output impedance block, is a combination between the grid impedance and a virtual impedance, and is used to calculate the output current based on the virtual voltage and the output voltage. Finally, the last block, calculates the positive and negative sequence of the output voltage and grid current by using a dual second-order generalized integrator (DSOGI), where these quantities are used to calculate the positive sequence voltage amplitude of the converter output voltage \hat{v}_o^+ , and of the reactive current i_Q^+ as shown in the figure.

Small-signal Model

To optimize the control parameters, the small-signal model of Fig. 1 is derived. The model consists of two parts, the plant part represents the physical components of the system, while the control part represents the active and reactive power control. The output impedance and the DSOGI build up the plant model, while the remaining blocks of Fig. 1 represent the controller part. For the small-signal model the converter is considered as an ideal part, i.e., the internal current and voltage control in addition to the semiconductor losses were not evaluated. Therefore, the converter is represented by an ideal AC voltage source which is connected to the grid through an impedance. In Fig. 2 a single-phase equivalent circuit of the system is presented in addition to the plant model. Fig. 3 shows the block diagram of the DSOGI, based on this a state space model of the DSOGI is implemented where the inputs are the grid current i_g and the converter output voltage v_o while the system exports

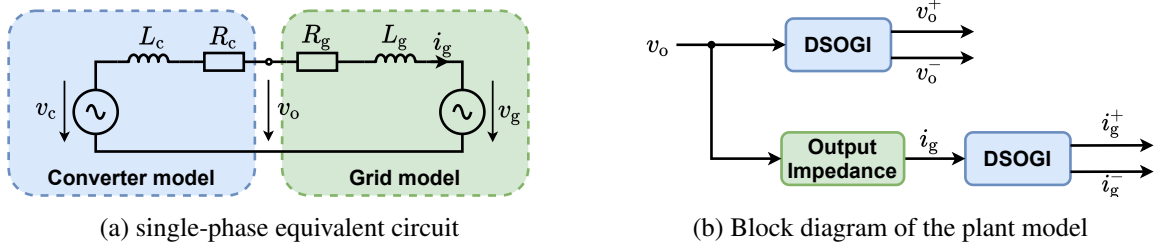


Fig. 2: Block diagram of the physical part of the small-signal model

the positive i_g^+ , v_o^+ and negative i_g^- , v_o^- sequence of the input quantities. This system is presented in equations (9) and (10), where ω is the fundamental frequency of the input signal and $k = \sqrt{2}$.

$$\begin{pmatrix} s \cdot v'(s) \\ s \cdot qv'(s) \end{pmatrix} = \begin{pmatrix} -\omega k & -\omega \\ \omega & 0 \end{pmatrix} \cdot \begin{pmatrix} v'(s) \\ qv'(s) \end{pmatrix} + \begin{pmatrix} \omega \\ 0 \end{pmatrix} \cdot v(s) \quad (9)$$

$$\begin{pmatrix} v^+(s) \\ v^-(s) \end{pmatrix} = \begin{pmatrix} 1/2 & j/2 \\ 1/2 & -j/2 \end{pmatrix} \cdot \begin{pmatrix} v'(s) \\ qv'(s) \end{pmatrix} \quad (10)$$

The grid impedance together with the virtual impedance used by the reactive power control represent the output impedance of the system. From the differential equation of the output impedance shown in equation (11), the small-signal model of the output impedance can be derived.

$$v_o(s) = s \cdot L_i \cdot i_g(s) + R_i \cdot i_g(s) + v_g(s) \implies s \cdot i_g(s) = \frac{R_i}{L_i} \cdot i_g(s) + (-1/L_i \quad 1/L_i) \cdot \begin{pmatrix} v_g(s) \\ v_o(s) \end{pmatrix} \quad (11)$$

The system of the plant model is then obtained by combining the models of the DSOGI and the output impedance. The acquired system consist of AC quantities which are represented in the complex domain. To apply the control strategies, the Park transform should be performed on the system. Moreover, the system must be transformed in to the real domain to describe the real physical system.

Besides the plant model which represents the physical part, the control model describes the applied active and reactive power control. For the reactive power, the strategy presented in [4] is used. This algorithm replaces the $Q \sim V$ -droop with a $-i_Q \sim V$ -droop, where i_Q is the reactive current. As a result, the control strategy provides voltage support similar to that required by grid-connected inverters [6] in existing grid codes. In addition to that, the $-i_Q \sim V$ -droop allows normal operation for deeper voltage sags at similar voltage support characteristic to the $Q \sim V$ -droop in the nominal range. Also, this strategy improves the linearity of the system due to the linear relationship between i_Q and V . According to Fig. 1 the positive sequence of the converter output voltage v_o^+ and grid current i_g^+ are used to calculate the positive sequence amplitude of the converter output voltage \hat{v}_o^+ and reactive current i_Q^+ . The difference between the calculated values and their reference values represent the input signals of the voltage controller, where a proportional-integral (PI) controller is used. The controller outputs the virtual voltage amplitude \hat{v}_v . Equation (12) shows the virtual voltage amplitude in addition to the PI-controller, k_{Qp} and k_{Qi} are the control parameters while k_Q defines the $-i_Q \sim V$ -droop.

$$\hat{v}_v = (k_{Qp} + \frac{k_{Qi}}{s}) \cdot (\hat{v}_o^+ - \hat{v}_{o,n}^+ - k_Q \cdot (i_Q^+ - i_{Q,n}^+)) \quad \text{with} \quad k_Q = 0.5 \cdot \frac{V_{o,n}}{I_n} \quad (12)$$

The active power control is ensured by applying the presented algorithm in equation (7). The power-to-frequency characteristic is shown in equation (8). During steady state, the PI-controller ensures zero steady-state deviation of the dc-link voltage. Based on that, equation (8) becomes similar to equation (1) which means that in steady-state, the behaviour of the converter matches that of the synchronous

generator. As it can be seen from the control equations the control system is not linear, therefore to build a small-signal model the equations need to be linearized around an operating point to calculate the system matrices. This operating point is chosen to be the nominal operating point of the converter (table II). After the linearization, the control model can be obtained by combining the active and reactive power control systems. Finally, the combination of the plant and control model produces a model that describes the system.

To perform stability analysis, the eigenvalues of the system matrix A of the obtained model must be calculated, where these eigenvalues are related to the control parameters. The matrix A is of order 15, which means that there are 15 eigenvalues.

For the stability analysis, a parameter sweep was performed, starting from a certain point, the parameters were changed to cover a specific range, and at each point, the eigenvalues were calculated and analysed. Due to the six control parameters and the high order of matrix A , the parameter sweep method is complex and the analysis of the results is fraught with difficulties. To reduce the complexity of the problem, the parameter k_4 is not swept. This parameter is the gain of the integrator to keep the dc-link voltage at its nominal value in the steady-state. The mentioned parameter has no significant influence on the stability of the system. It only affects the time needed for the dc-link voltage to reach its nominal value after a disturbance of the system. From the simulation results shown later, a value of $k_4 = 0.08 \text{ A}^2 \text{ s J}^{-2}$ gives a good compromise between the control time and the overshoot of the dc-link voltage. For further reduction of complexity, the sweep is performed for each parameter individually after selecting the optimal value, the next parameter will be swept. The sweep start from the following parameters:

$$k_1 = -90 \text{ s}^{-1}; \quad k_2 = 1.2 \text{ J}^{-1} \text{ s}^{-1}; \quad k_3 = 0.02 \text{ A}^2 \text{ J}^{-2}; \quad k_{Qi} = -17; \quad k_{Qp} = 0.4 \quad (13)$$

The first parameter that swept is k_2 . The movements of the eigenvalues is shown in Fig. 4b. The analysis shows that the eigenvalues 1,2,3,4,7 and 8 are not changed by the shift Whereas, the eigenvalues 5,6,9 and 10 are slightly affected by the variation of k_2 . These poles move away from the origin of the coordinate system with a decreasing imaginary part. This improves the damping and response of the system. On the other hand, 11 and 12 shift to the left in the coordinate system when k_2 is increased. This shift enhances the stability of the system. However, eigenvalues 13, 14 and 15 become unstable when k_2 becomes too large. Equation (8) shows that the parameter k_2 is inversely proportional to the emulated inertia. Hence, if k_2 is too large, the emulated inertia will be minimal. As a result, the system response becomes too fast, and damping decreases. Conversely, if the value of k_2 is small, the emulated inertia is large, and cannot be realized due to the significant drop of the dc-link voltage, which will cause large-signal instability. The optimal value is chosen so that the system has the best damping and fast response. This is achieved by placing most of the eigenvalues on the real axis. For $k_2 = 1.3 \text{ J}^{-1} \text{ s}^{-1}$, eigenvalues 13, 14, and 15 have an imaginary part of zero. The remaining poles are well-damped and fast.

Secondly, k_1 will be swept, with a range from 0 to -150 s^{-1} . The loci of the eigenvalues are shown in Fig.4a. Similar to k_2 , the poles 1,2,3,4,7 and 8 are not affected by the shift. On the other hand, eigenvalues 5,6,9 and 10 tend to shift toward the origin of the coordinate system when k_1 is decreased. However, these poles become better damped. Moreover, poles 11 and 12 start near the origin and move to the left when k_1 decreases. Nevertheless, both poles move back to the origin when $k_1 \leq -95 \text{ s}^{-1}$. Furthermore, eigenvalues 13, 14 and 15 remain on the real axis when k_1 decreases. A comparison between equation (8) and (1) shows k_1 is proportional to the damping parameter D_{SG} . This means that with a higher value of k_1 , the system is better damped. This behavior is also shown in Fig.4a, where the imaginary part of the eigenvalues becomes smaller with larger value of k_1 . Even so, when the damping factor is too high, the system becomes unstable. As with k_2 , the optimal value is chosen to achieve the best damping and fast response. A value of $k_1 = -110 \text{ s}^{-1}$ satisfies the requirements. At this value, eigenvalues 11 and 12 occupy the most stable point. Where poles 13,14 and 15 settle on the real axis.

The parameters k_1 and k_2 are responsible for the synchronization of the grid and the control of the active power. After tuning these parameters, the reactive power control is now optimized by finding the optimal values for k_{Qp} and k_{Qi} . Fig. 5a shows the loci of the eigenvalues when k_{Qp} is modified. The eigenvalues 1,2,3,4,7 and 8 are not affected by the sweep of the parameter. However, as can be seen in Fig. 5a, the

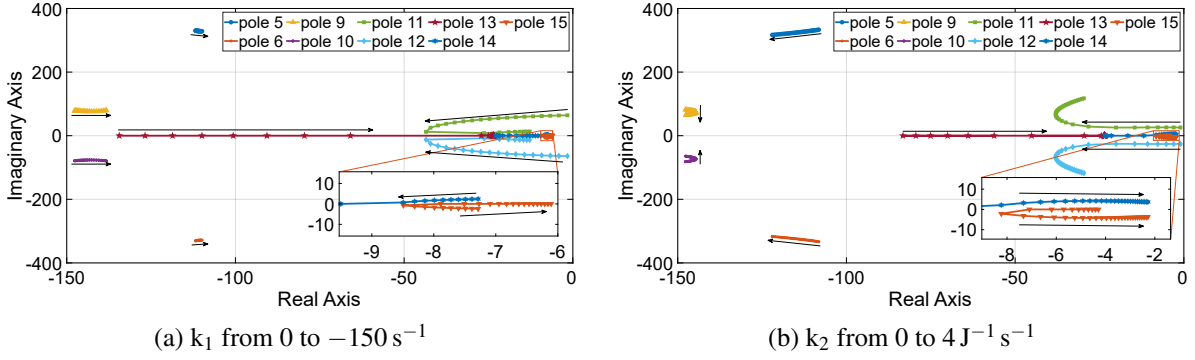


Fig. 4: Small signal model stability analysis active power controller

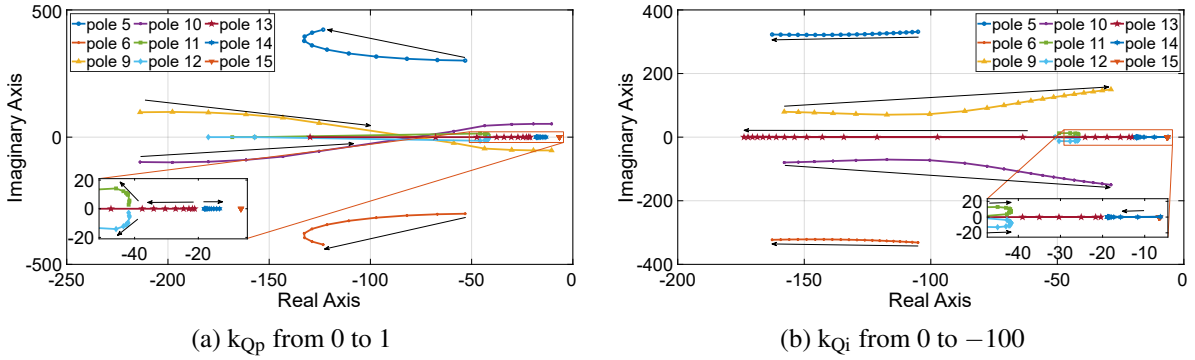


Fig. 5: Small signal model stability analysis reactive power controller

parameter k_{Qp} has a significant influence on the stability of the system. The eigenvalues 5 and 6 shift to the left of the origin at higher values of the parameter, which improves the system's response. However, the imaginary part of these two poles becomes more significant, and thus these eigenvalues become less damped. In addition, eigenvalues 11, 12 and 13 become faster when k_{Qp} is increased, the damping of these poles is not significantly affected. On the other hand, the remaining eigenvalues tend to become unstable when k_{Qp} becomes larger.

The parameter k_{Qp} is the gain of the proportional part of the virtual voltage controller. Through this parameter, the system's response to voltage sags is defined. The optimal value for this parameter should be a good compromise between fast response, and a good damping. A value of $k_{Qp} = 0.4$ achieves this requirement. At this value, the poles 9, 10 and 13 are on the real axis, and the remaining eigenvalues are well damped.

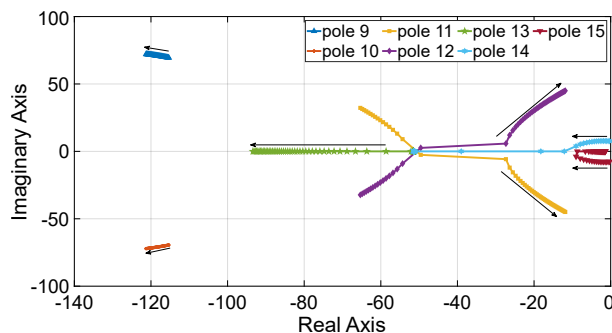


Fig. 6: k_3 from 0 to $0.03 \text{ A}^2 \text{ J}^{-2}$

Besides k_{Qp} , the parameter k_{Qi} also influences the system behavior in case of voltage sag. This parameter is the integrator part of the virtual voltage controller. Figure 5b shows the locus of eigenvalues. Also, for this parameter, eigenvalues 1, 2, 3, 4, 7 and 8 are not affected. However, poles 9 and 10 become slower and less damped by higher values of k_{Qi} . In contrast, the remaining poles improve their behaviour as the parameter is increased. Just as for k_{Qp} , an optimum is chosen to obtain the best damping and good system performance. The chosen value is $k_{Qi} = -30$.

Finally, the last parameter swept is k_3 . This parameter is responsible for the tracking of the dc-link voltage. In Fig. 6, the loci of the eigenvalues are presented. Only the poles from 9 to 15 are affected by the modified parameter. As shown in Fig. 6,

the poles 9, 10, 13 and 14 improve the stability of the system when the parameter increases. However, the other eigenvalues move towards unstable positions.

The optimum value for this parameter is $k_3 = 0.02 \text{ A}^2 \text{ J}^{-2}$. At this value, the poles from 13 to 15 are on the real axis, which improves the damping of the system. The obtained control parameters are used in a large-scale simulation and for the measurements, the corresponding results are presented in the next sections. In summary the parameters determined by the above procedure are:

$$k_1 = -110 \text{ s}^{-1}; \quad k_2 = 1.3 \text{ J}^{-1} \text{ s}^{-1}; \quad k_3 = 0.02 \text{ A}^2 \text{ J}^{-2}; \quad k_{Qi} = -30; \quad k_{Qp} = 0.4 \quad (14)$$

Simulation results

To show the benefits of the optimized control, a large-signal model is built in Matlab/Simulink which compares the two control strategies. A line-to-line fault with line impedance to fault impedance ratio of 1:4 is simulated, which shows the performance of both strategies for an unbalanced fault. As expected, the dc-link voltage of both control schemes shows the 100 Hz oscillation that is caused by the unbalanced fault (Fig. 7b). Additionally, the optimized control leads to a higher overshoot of the dc-link voltage, which is caused by the integral part of the controller. However, in the standard control strategy, the dc-link voltage deviates from its reference value. On the other hand, comparing the frequency response shows the benefits of the optimized control, which eliminates most of the frequency oscillations that are present in the standard strategy (Fig. 7a). To validate the simulation results, the proposed strategy is

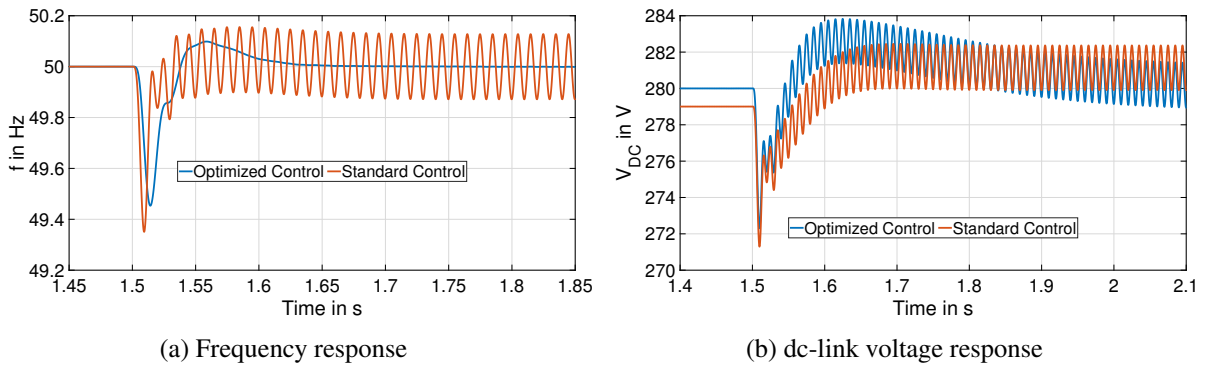


Fig. 7: Comparison of the two control schemes during a line-to-line grid fault

tested under different grid conditions. The measurement results will be shown in the following section.

Measurement results

The test bench used to perform the experiments consists of three two-level converters, which can operate independently or in a parallel circuit. In addition, these converters can feed a passive load or be connected to a grid emulator. Fig. 8 depicts the setup of the test bench, and the system parameters are listed in table II. The devices used to perform the measurements are listed in table I.

Nominal dc-link Voltage	$V_{DC,n} = 309\text{ V}$	dc-link Capacitor	$C_{DC} = 2.2\text{ mF}$
Nominal RMS Output Voltage	$V_{o,n} = 70\text{ V}$	Filter Capacitor	$C_f = 16\mu\text{F}$
Nominal RMS Current	$I_n = 9.5\text{ A}$	Converter side Inductance	$L_{fC} = 5.6\text{ mH}$
Nominal Power	$P_n = 2000\text{ W}$	Grid side Inductance A	$L_{fg,A} = 2.93\text{ mH}$
Nominal Frequency	$f_n = 50\text{ Hz}$	Grid side Inductance B	$L_{fg,B} = 0\text{ mH}$
Switching Frequency	$f_s = 3200\text{ Hz}$	Grid side Inductance C	$L_{fg,C} = 0.73\text{ mH}$

Table II: List of the converter's nominal values

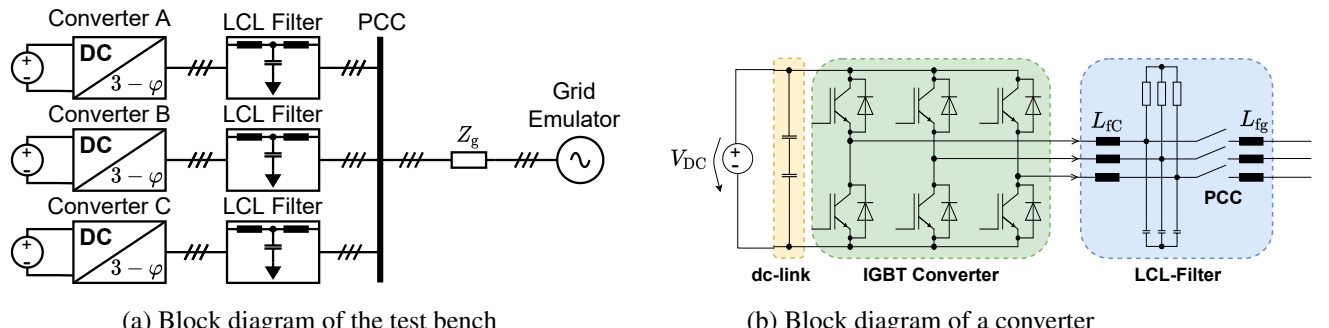


Fig. 8: Photo of the measurement setup

1	Converter A	6	dSPACE MicroLabBox
2	Converter B	7	PCC Switching Box
3	Converter C	8	DC Power Source: EA-PS 91000-30
4	Grid Side Inductance $L_{fg,A}$ and $L_{fg,C}$	9	Grid Emulator: Cinergia GE+EL-30
5	Common Mode Choke	10	HIL: OP5600 HIL Box

Table I: List of the used hardware

For a better understanding of the test bench, Fig. 9 shows a block diagram of the whole system, in addition to the structure of one converter. Each converter is connected to the grid emulator via an **LCL** filter. Except for the grid side filter inductor L_{fg} , the three inverters and filters are identical. The control software is implemented in MATLAB/Simulink, and the hardware is controlled via a dSPACE MicroLabBox.



(a) Block diagram of the test bench

(b) Block diagram of a converter

Fig. 9: Test bench setup

Unbalanced grid faults

To validate the simulation results, a line-to-line fault with a line impedance to fault impedance ratio of 1:4 is simulated. During this experiment, converter A is connected to the grid emulator (Cinergia GE+EL-30) that simulates the fault. The experimental results are shown in Fig. 10. The dc-link voltage shows the expected 100 Hz oscillation during the grid fault. However, this oscillation is not present in the frequency response due to the notch filter. Moreover, the new PID-controller regulates the dc-link voltage to its reference value, and the system shows a stable and well-damped behavior. This test shows that the control strategy can work under unbalanced grid conditions without the frequency suffering from oscillations.

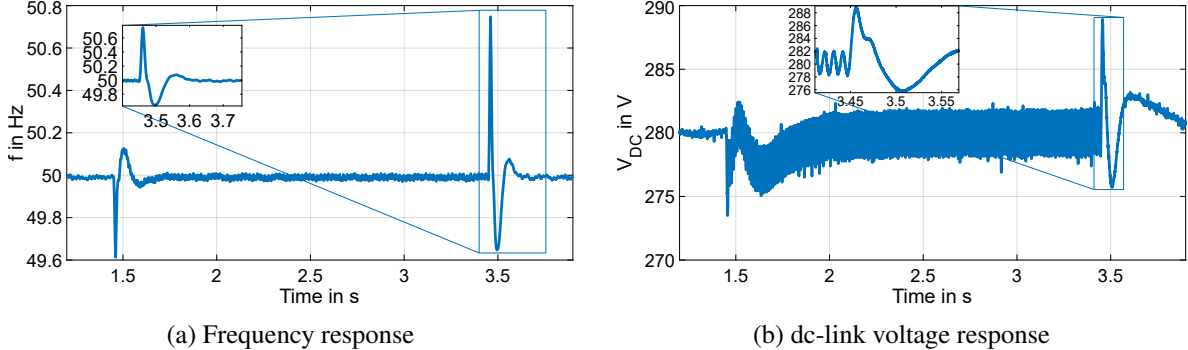


Fig. 10: Response of the proposed control strategy during grid fault

Islanded operation mode

In this test, the focus is on the ability of the proposed control strategy to operate within networks of converters with different control algorithms and the interaction between these control strategies. For this purpose, the three converters were connected in parallel to create an islanded grid. In this grid, converters A and B operate with the proposed control strategy, while converter C performs a grid-forming (GFM) droop control. It is important to note that, both converters A and B have no DC power source and balance power fluctuation using the dc-link only, which will provide minimum frequency support to the grid. To investigate the effects of this minimum support on the grid, load steps were simulated, and the results are shown in Fig. 11a. To demonstrate the effect of the control strategy, converter C was tested separately

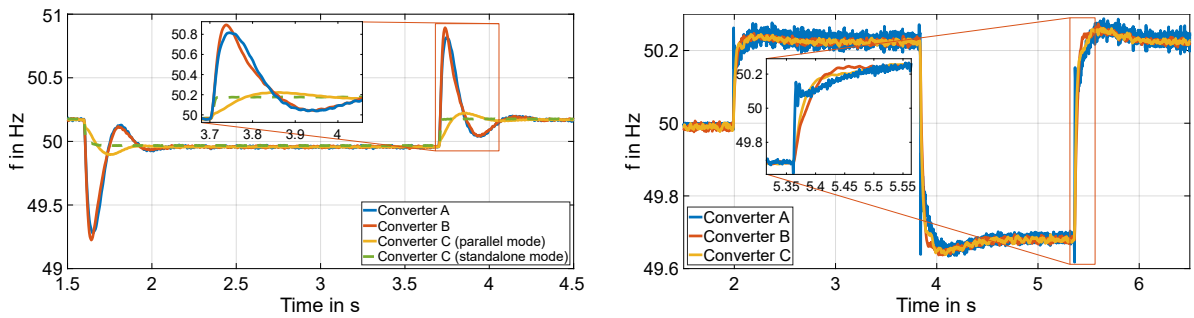


Fig. 11: System behavior during parallel connection

with the same load step (green curve in Fig. 11a). As can be seen in the figure, the system operates stably during the load change. To evaluate the effects of the minimum inertia support provided by converters A and B, the frequency of converter C is considered in parallel and standalone mode. The frequency change of converter C in parallel operation is slower than in standalone operation, indicating that the rate of change of frequency (RoCoF) is reduced, due to the increase in total system inertia. On the other hand, a small overshoot of the frequency during parallel connection is also present. This overshoot

comes from the fact that the matching control adapts the dc-link voltage, which forces the droop control to briefly provide more or less power than is required by the load. The inverter inertia constant provides an indication of the inertia added to the system by the control strategy used. Per definition, the inertia constant is calculated as follows:

$$H = \frac{E}{S_n} \quad E = \frac{1}{2} \cdot C_{DC} \cdot U^2 \quad U = V_{DC,min} + \Delta V_{DC} \quad S_n = 2000 \text{ VA} \quad (15)$$

where E is the available energy stored in the dc-link capacitor, and S_n is the nominal apparent power of the converter. For the used setup, the minimal dc-link voltage is $V_{DC,min} = 220 \text{ V}$ and the acceptable deviation is $\Delta V_{DC} = 100 \text{ V}$. With these values, the converter inertia constant is $H = 30 \text{ ms}$.

Another test was performed in parallel mode, where converters B and C apply the proposed strategy, while converter A operates in grid-following (GFL) mode. The objective of this test is to prove the ability of the control strategy to establish a stable grid where GFL control strategies can operate well. The same load step as in the previous test was performed, the results are shown in Fig. 11b. The GFL strategy operates stably in this parallel connection, with the frequency of converter A following that of converters B and C. However, it can also be seen that the frequency of converter A fluctuates slightly at the moment of load jump, which is caused by the weak grid conditions. Likewise, it is noticeable that the frequency of converter A changes faster than the frequencies of the other converters at the moment of the step, but slows down later and follows the frequency of converters B and C. This behavior is due to a phase jump associated with the load step, which causes some stability problems for the PLL.

Conclusion

This paper proposes an optimized grid-forming control strategy that can successfully operate under unbalanced faults and weak grid conditions. Moreover, the benefits of utilizing the dc-link capacitor as an energy source to deliver minimal inertia support have been investigated. A small-signal model of the system has been derived and used to optimize the control parameters. The system is then tested under different conditions. These tests have shown that the strategy remains stable during unbalanced faults. In addition, the minimum inertial support added by the proposed control strategy contributes to the reduction of RoCoF.

References

- [1] I. Cvetkovic, D. Boroyevich, R. Burgos, C. Li and P. Mattavelli, "Modeling and control of grid-connected voltage-source converters emulating isotropic and anisotropic synchronous machines," 2015 IEEE 16th Workshop on Control and Modeling for Power Electronics (COMPEL), 2015, pp. 1-5, doi: 10.1109/COMPEL.2015.7236454.
- [2] L. Huang et al., "A Virtual Synchronous Control for Voltage-Source Converters Utilizing Dynamics of DC-Link Capacitor to Realize Self-Synchronization," in IEEE Journal of Emerging and Selected Topics in Power Electronics, vol. 5, no. 4, pp. 1565-1577, Dec. 2017, doi: 10.1109/JESTPE.2017.2740424.
- [3] A. Tayyebi, D. Gro, A. Anta, F. Kupzog and F. Drfler, "Frequency Stability of Synchronous Machines and Grid-Forming Power Converters," in IEEE Journal of Emerging and Selected Topics in Power Electronics, vol. 8, no. 2, pp. 1004-1018, June 2020, doi: 10.1109/JESTPE.2020.2966524.
- [4] M. Eggers, H. Yang, H. Just and S. Dieckerhoff, "Virtual-Impedance-Based Droop Control for Grid-Forming Inverters with Fast Response to Unbalanced Grid Faults," 2020 IEEE 11th International Symposium on Power Electronics for Distributed Generation Systems (PEDG), 2020, pp. 122-129, doi: 10.1109/PEDG48541.2020.9244440.
- [5] Peter Unruh et al."Overview on Grid-Forming Inverter Control MethodsIn: Energies 13.10 (2020). issn: 1996-1073. doi: 10.3390/en13102589. url: <https://www.mdpi.com/1996-1073/13/10/2589>.
- [6] Summary of the draft VDE-AR-N 4110:2017-02, 2017.
- [7] H. Just, H. Yang and S. Dieckerhoff, "Evaluation of Advanced PLL Concepts for Enhanced Fault Ride Through Response," 2018 IEEE Energy Conversion Congress and Exposition (ECCE), 2018, pp. 5684-5691, doi: 10.1109/ECCE.2018.8558444.
- [8] Global wind statistics 2017, Global Wind Energy Council, Tech. Rep., 2018.
- [9] F. Milano, F. Drfler, G. Hug, D. J. Hill and G. Verbi, "Foundations and Challenges of Low-Inertia Systems (Invited Paper)," 2018 Power Systems Computation Conference (PSCC), 2018, pp. 1-25, doi: 10.23919/PSCC.2018.8450880.